

# Anisotropic shock response of titanium: Reorientation and transformation mechanisms

Hongxiang Zong<sup>a,b</sup>, Turab Lookman<sup>b,\*</sup>, Xiangdong Ding<sup>a,\*</sup>,  
Sheng-Nian Luo<sup>c</sup>, Jun Sun<sup>a</sup>

<sup>a</sup> State Key Laboratory for Mechanical Behavior of Materials, Xi'an Jiaotong University, Xi'an 710049, People's Republic of China

<sup>b</sup> Theoretical Division, Los Alamos National Laboratory, Los Alamos, NM 87545, USA

<sup>c</sup> Peac Institute of Multiscale Sciences and Sichuan University, Chengdu, Sichuan 610207, People's Republic of China

Received 24 September 2013; received in revised form 14 November 2013; accepted 17 November 2013

Available online 20 December 2013

## Abstract

We investigate shock-induced phase transformations in titanium ( $\alpha$ -Ti) single crystals induced by shock loading along the [0001], [10 $\bar{1}$ 0] and [12 $\bar{1}$ 0] directions using molecular dynamics simulations. We find a significant dependence of the microstructure evolution on the crystallographic shock direction, providing insight into the nature of the coupling between deformation and phase transformation. For shock along the  $c$ -axis, the orientation relationships (ORs)  $(0001)_\alpha // (10\bar{1}0)_\omega$  and  $[10\bar{1}0]_\alpha // [11\bar{2}3]_\omega$  between parent and product phases are observed, which differs from that previously reported for Ti. For shock compression along the [10 $\bar{1}$ 0] and [12 $\bar{1}$ 0] directions, there is a reorientation of the hexagonally close-packed  $\alpha$  phase before the  $\alpha \rightarrow \omega$  martensitic transformation, and the OR is consistent with the previously proposed Silcock relationship. We associate the reorientation with a shuffle and shear mechanism and suggest that shear stress is an underlying factor for the anisotropic phase transformation sensitivity.

© 2013 Acta Materialia Inc. Published by Elsevier Ltd. All rights reserved.

**Keywords:** Shock compression; Martensitic transition; Titanium; Orientation relationships

## 1. Introduction

The group IV transition metal titanium (Ti) is amongst the most desirable of candidate materials due to its widespread and successful applications in the aerospace, nuclear and biomedical industries [1–4]. The allotropic phase transitions in pure Ti sensitively depend on tunable thermodynamic parameters such as external pressure and temperature. In particular, the pressure-induced martensitic hexagonally closed-packed (hcp)  $\alpha$  to hexagonal  $\omega$  transformation is important because  $\omega$  phase formation affects toughness and ductility of Ti. This martensitic phase transformation can occur in  $\alpha$ -Ti under hydrostatic, shock

loading or high-pressure torsion conditions [5–7]. The room temperature (RT)  $\alpha \rightarrow \omega$  phase transformation has been observed to occur at between 2 and 12 GPa, depending on the experimental technique, the pressure environment and the sample purity [8–12]. Furthermore, unlike the  $\alpha \rightarrow \epsilon$  transformation in pure Fe, the  $\alpha \rightarrow \omega$  transformation in Ti exhibits a large hysteresis that is responsible for retention of the metastable high-pressure  $\omega$  phase on release to atmospheric pressure [5,6,8].

Transmission electron microscopy (TEM) has been extensively used to understand the crystallography of the  $\alpha \rightarrow \omega$  transformation. As this transformation is accompanied by hysteresis and can be irreversible, the high-pressure hexagonal  $\omega$  phase can be retained partially or almost fully after unloading under ambient conditions [7]. Although this is well established under both static and shock conditions, the crystallographic nature of the transformation in Ti and Zr is still controversial [11,13–16]. In particular, it

\* Corresponding authors. Tel.: +1 505 665 0419 (T. Lookman).  
Tel.: +86 13379200208 (X. Ding).

E-mail addresses: [txl@lanl.gov](mailto:txl@lanl.gov) (T. Lookman), [Dingxd@mail.xjtu.edu.cn](mailto:Dingxd@mail.xjtu.edu.cn) (X. Ding).

is not clear how the orientation relationships (ORs) depend on loading conditions. Moreover, little is understood about the coupling of deformation processes to phase transformation. Textural analysis below and above the phase transformation pressure suggests microstructural reorientation [11]; however, the nature of deformation twinning or dislocation slip mediating the transformation is not clear. Measurements to date have been primarily on polycrystalline samples and the anisotropy in shock response is not easily inferred from these measurements. Thus, our focus here is on studying the anisotropic response in single crystals, thereby providing insight into the factors mediating the phase transformation. We also suggest the types of measurements that can corroborate our findings.

ORs are key signatures of pathways that lead to a given microstructure. Essentially three ORs between the starting  $\alpha$  and final  $\omega$  phase have been observed so far in TEM studies of polycrystalline samples of Zr and Ti under different loading conditions. These are the so-called Variant I with the ORs  $(0001)_\alpha // (10\bar{1}1)_\omega$  and  $[10\bar{1}0]_\alpha // [\bar{1}011]_\omega$ , Variant II with the ORs  $(0001)_\alpha // (1\bar{2}10)_\omega$  and  $[1\bar{2}10]_\alpha // [0001]_\omega$ , and the form proposed by Song and Gray [14] or Variant III with the ORs  $(0001)_\alpha // (10\bar{1}0)_\omega$  and  $[10\bar{1}0]_\alpha // [11\bar{2}3]_\omega$ . The first two were initially proposed by Usikov and Zilbershtein on the basis that the  $\alpha \rightarrow \omega$  transformation occurs via an intermediate  $\beta$  phase [17]. Variant I has been primarily observed in hydrostatic and steady-state pressure conditions in both Zr and Ti in the pressure range 2.9–9 GPa at RT [14]. This OR was also later observed by Vohra et al. in dilute Ti–V alloys [18]. Variant II has been observed in pressure-treated Zr samples by Rabinkin et al. via electron diffraction measurements [19]. In pressure studies of Ti alloys, Silcock observed a direct  $\alpha \rightarrow \omega$  transformation pathway for which the OR is the same as Variant II [20]. Note that although this OR is the same as Variant II, the pathways are quite distinct. Over the last few years, the availability of computing power has made feasible the enumeration of atomic pathways in crystals, especially for non group–subgroup transformations such as in Ti and Zr. Following this prescription, Trinkle et al. enumerated the lowest-energy pathways in Ti under hydrostatic pressure and discovered a direct pathway (TAO-1) with a lower energy than that noted by Silcock. This pathway has the same OR as Variant I [16]. Recently, there have been a number of studies involving high-pressure torsion (HPT) measurements on polycrystal Zr and Ti. The loading conditions favor shear-driven transformations leading to almost complete transformation to the  $\omega$  phase. However, the mechanism has not been particularly well studied, although it has been suggested that the OR is consistent with TAO-1 [8]. There have been a number of studies of the ORs on shocked samples of Zr polycrystals. These studies largely find the same OR as Variant II [21]. The exception is the analysis by Song and Gray [14] who observed Variant III [11,14] and also proposed a specific pathway. This OR has been recently re-examined with the conclusion that it is a subset of Variant I [15].

Our objective here is to investigate how the ORs and transformation pathways are influenced if a Ti single crystal is shocked in different directions. Moreover, in order to explain the range of behavior seen in the above experiments, we study the effects on the phase transformation of the deformation behavior during shock compression and the anisotropy of the shock response. We find that loading along the  $c$ -axis gives rise to the ORs  $(0001)_\alpha // (10\bar{1}0)_\omega$  and  $[10\bar{1}0]_\alpha // [11\bar{2}3]_\omega$ , which have not been observed previously though are related to the ORs seen in shocked polycrystal samples of Zr [14]. However, under shock compression along the  $a$ -axis, the  $\alpha$ -Ti crystal experiences first an effective 90° rotation, which is induced by a shear and shuffle (or atomic displacement mode) mechanism. This is followed by the  $\alpha \rightarrow \omega$  phase transformation. The OR is consistent with the Silcock relationship or Variant II, and the pathway is the same as Silcock. We suggest that shear is an underlying factor responsible for the anisotropic phase transformation sensitivity.

## 2. Computational method

The molecular dynamics (MD) simulations were carried out using the Large-scale Atomic/Molecular Massively Parallel Simulator (LAMMPS) code [22] and a Ti modified embedded atom method (MEAM) potential with a cubic-splines-based functional form [23]. This potential removes the constraint of fixed angular character and allows for additional flexibility of the potential compared with traditional MEAM potentials. The EAM views each atom as embedded in a host lattice consisting of all other atoms. Each atom in the system is viewed as an impurity that is part of a host of all other atoms. The “embedding energy” of the impurity is determined by the electron density of the host before the impurity is added. The energy of an atom (or impurity) is represented as a two-body energetic interaction plus an embedding energy computed on the basis of an empirical electron density. Incorporating angular terms in the EAM density functional has led to the development of spline-based MEAM:

$$E_i = \frac{1}{2} \sum_j \phi(r_{ij}) + U(\rho_i), \quad (1)$$

with the density at atom  $i$  given by:

$$\rho_i = \sum_j \rho(r_{ij}) + \sum_{jk} f(r_{ij}) f(r_{ik}) g[\cos(\theta_{jik})], \quad (2)$$

where  $\phi(r_{ij})$  is a direct two-body interaction between atoms  $i$  and  $j$  that depends only on the interatomic separation  $r_{ij}$ . The total effective electron density  $\rho_i$  at atomic site  $i$  contributes to the total system energy through the embedding function  $U(\rho_i)$ . The density  $\rho(r_{ij})$  represents the contribution to the total effective electron density at atom  $i$  due to atom  $j$  a distance  $r_{ij}$  away. A radial cutoff function  $f(r)$  and a three-body angular term  $g(\cos(\theta))$  is used to describe

the three-body effect on the total effective electron density.  $\theta_{jik}$  is the angle between atoms  $i, j$  and  $k$  centered on atom  $i$ . The five functions  $\phi(r)$ ,  $U(\rho)$ ,  $\rho(r)$ ,  $f(r)$  and  $g(\cos(\theta))$  are represented by cubic splines, and the spline parameters are fitted by lattice constants, elastic moduli, and cohesive and surface energies.

The simulation presented in this study focuses on the  $\alpha \rightarrow \omega$  martensitic transformation in perfect Ti mono-crystalline slabs of dimensions  $L_x = L_y = 24$  nm and  $L_z = 160$ – $200$  nm. Before impact the crystalline structure of the target material is  $\alpha$ -Ti. The  $z$  axis, parallel to the  $[0001]$ ,  $[10\bar{1}0]$  or  $[1\bar{2}10]$  crystallographic directions of the  $\alpha$ -Ti crystal, is chosen as the impact direction. Periodic boundary conditions are imposed in the  $x$  and  $y$  directions, while the target has two free surfaces perpendicular to the  $z$  axis. The impactors have the same cross-section 30 nm in length and an initial impact speed of  $0.9$  km s $^{-1}$ —see Fig. 1a. Altogether the target and the impactor contain approximately 8 million atoms. Prior to compression, the specimens were first equilibrated to achieve a minimum energy state and the initial temperature was set at 30 K. In addition, the time step for integrating the equations of motion is 1 fs, and the shock run durations are up to 32 ps. The dependence of the shock wave velocity ( $u_s$ ) on the particle velocity ( $u_p$ ) is shown in Fig. 1b. The  $u_s$ – $u_p$  relations for the  $[0001]$ ,  $[10\bar{1}0]$  and  $[1\bar{2}10]$  shock simulations are presented. The MD data for single crystals were fitted to the linear  $u_s$ – $u_p$  relation and this was compared to that from polycrystalline experimental results [24] for Ti in the  $u_p$  velocity range 0–2.0 km s $^{-1}$  in all three orientations. While it is still unclear how to construct a polycrystalline Hugoniot from the single-crystal Hugoniot, our parameterization of the MD results for single-crystal Ti shows reasonable agreement with the experimental data.

### 3. Results and discussion

#### 3.1. Shock wave propagation in pure Ti single crystals

Wave profile measurements and interpretation play a central role in shock physics research. Theoretically, much information about the dynamic material response can be deduced from a wave profile. A more common type of profile for a solid has a two-wave or elastic–plastic wave feature, whereas a shocked solid may demonstrate a three-wave structure, i.e. elastic–plastic phase-change wave fronts. A three-wave structure may become a two-wave one if the plastic wave overtakes the elastic wave. In experiments, the shock wave profiles are measured using VISAR (velocity interferometer system for any reflector) which records the continuous motion at the back surface of the sample undergoing shock compression and release. The advantage of this diagnostic is that it measures both the structure of the shock wave as well as the shock transit time, and thus the shock speed. Phase transformations and spall phenomena are two examples of processes which manifest themselves in the wave profile structure [25–27].

Fig. 2 illustrates particle wave velocity profiles of pure Ti single crystals at three times, for (i) the  $[0001]$ , (ii) the  $[10\bar{1}0]$  and (iii) the  $[1\bar{2}10]$  orientations shock loaded at  $u_p = 900$  m s $^{-1}$ . The rigid piston is to the left in Fig. 2 and the wave front propagates to the right-hand side. The profiles are similar to those from experimental measurements using VISAR [26]. Note that a two-wave profile, which consists of an overdriven plastic front [28] and a transformation front, exists for the  $[1\bar{2}10]$  orientation shock loading but does not lead to a three-wave front structure. On the other hand, for the shock along  $[0001]$  and  $[10\bar{1}0]$ , the front splits into an elastic precursor, a plastic front and a phase transformation front, as shown in Fig. 2.

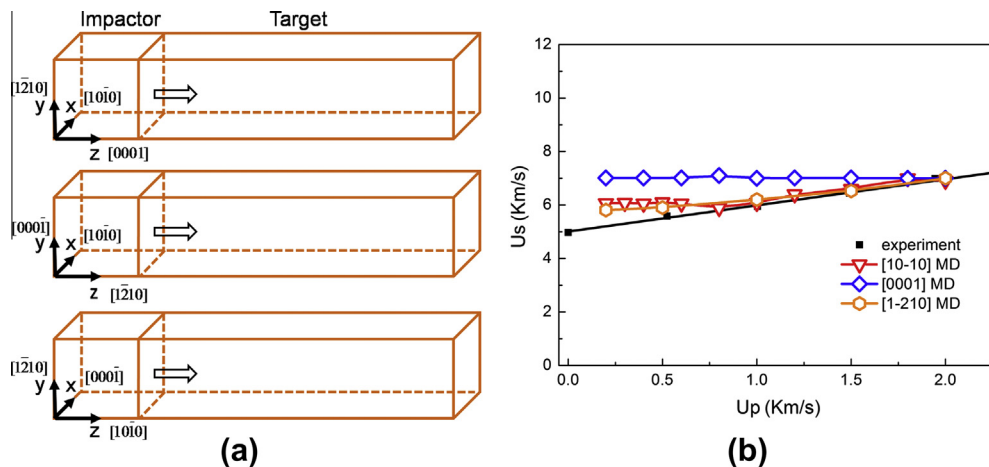


Fig. 1. (a) Molecular dynamics simulation setup showing shock-wave propagation along three perpendicular directions  $[0001]_z$ ,  $[10\bar{1}0]_z$  and  $[1\bar{2}10]_z$ . (b) Single-crystal Hugoniot results for the above three crystallographic shock orientations obtained from our simulations. The black squares refer to experimental polycrystalline data for Ti [24].

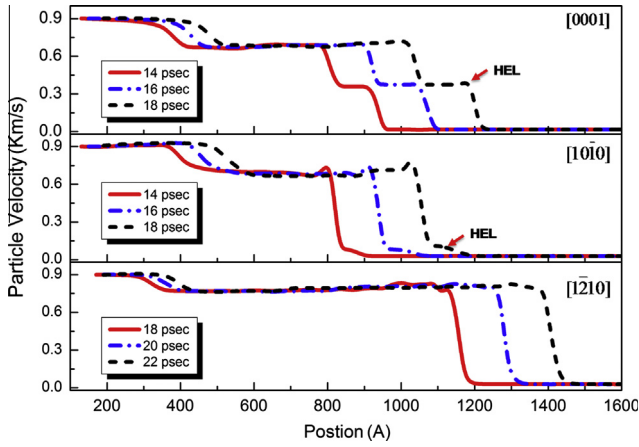


Fig. 2. Particle velocity profiles for shocks along the three crystallographic orientations as obtained from our simulations with piston velocity  $u_p = 900 \text{ m s}^{-1}$ . The shock front velocity,  $u_s$ , is obtained by following the drops in the particle velocities as a function of distance for split three-wave and two-wave structures as shown here for  $[0001]_x$ ,  $[10\bar{1}0]_x$  and  $[1\bar{2}10]_x$  directed shocks. HEL represents the Hugoniot elastic limit.

A closer look reveals a large dependence of the evolving microstructure on the crystallographic shock direction (Fig. 3). For shocks in the  $[0001]$  direction, the evolving

grains consist mostly of the  $\omega$  structure precipitated in the  $\alpha$  matrix and are relatively large, as shown in Fig. 3a and b. Here, three  $\omega$  variants of the product phase are observed that are separated by grain boundaries (incoherent twin boundaries). In contrast, the evolving microstructure for shocks in the  $[10\bar{1}0]$  and  $[1\bar{2}10]$  directions is more complex. Here a variant reorientation process of  $\alpha$ -Ti takes place before the phase transformation. For shock loading along the  $[10\bar{1}0]$  orientation, all the hcp first reorients to the  $[0001]$ -hcp variant, as shown in Fig. 3c and d, and then transforms to  $\omega$ . However, Fig. 3e for shock direction  $[1\bar{2}10]$  shows interfaces that in general have more curvature between the rotated and the unrotated regions than Fig. 3c. This is related to the presence of more than one rotated hcp variant for the  $[1\bar{2}10]$  direction shock compression.

### 3.2. Shock-induced $\alpha \rightarrow \omega$ transformation along the $c$ -axis

Fig. 3a shows an atomic configuration from a typical cross-section microstructure of the Ti sample following shock along  $[0001]$ . The  $\alpha$  matrix with precipitated  $\omega$  phase is seen to contain incoherent twin boundaries, consistent with the Zr polycrystalline shock experimental

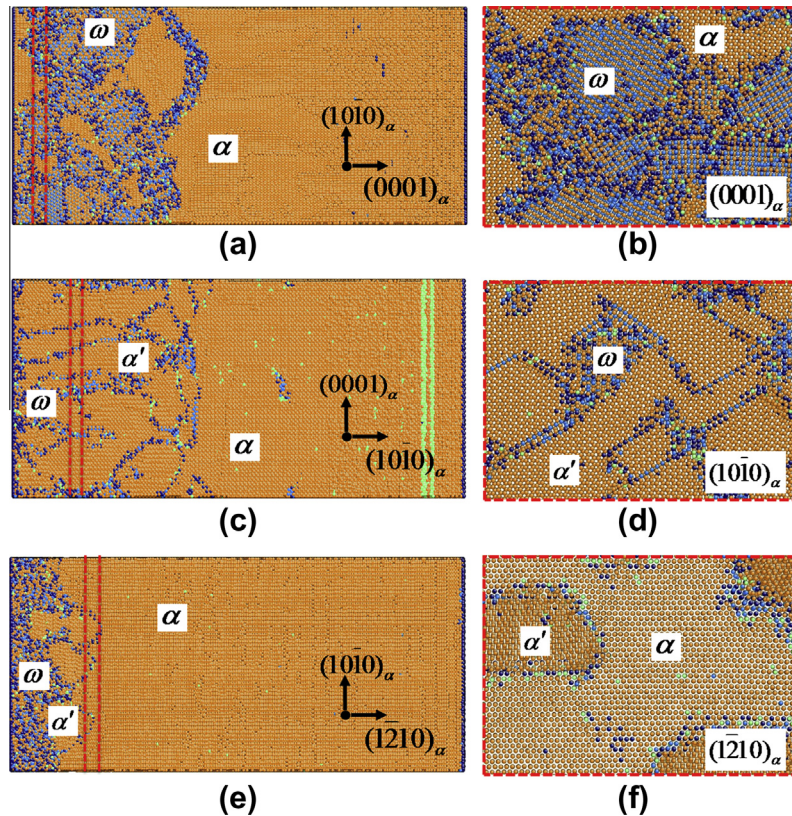


Fig. 3. Microstructure shocked along the three directions  $[0001]_x$ ,  $[10\bar{1}0]_x$  and  $[1\bar{2}10]_x$  after 8 ps. In the left panels (a), (c), (e), the shock direction is from the left to the right. The right panels (b), (d) and (f) show the configurations corresponding to the transverse cross-sections at the vertical bars in the panels (a), (c), (e), respectively. The orange and the blue (also blue stacking) colors represent the hcp  $\alpha$  phase and the hexagonal  $\omega$  phase, respectively. The reoriented parent  $\alpha$  phase is represented by  $\alpha'$ . We note that shock along  $[0001]_x$  leads only to phase transformation without any reorientation of the parent  $\alpha$ . Shocks along the other two directions first induce a reorientation of the parent  $\alpha$  to  $\alpha'$ , which then transforms to the  $\omega$  phase. The green vertical bars correspond to the elastic precursor in Fig. 2b. (For interpretation of the references to color in this figure legend, the reader is referred to the web version of this article.)

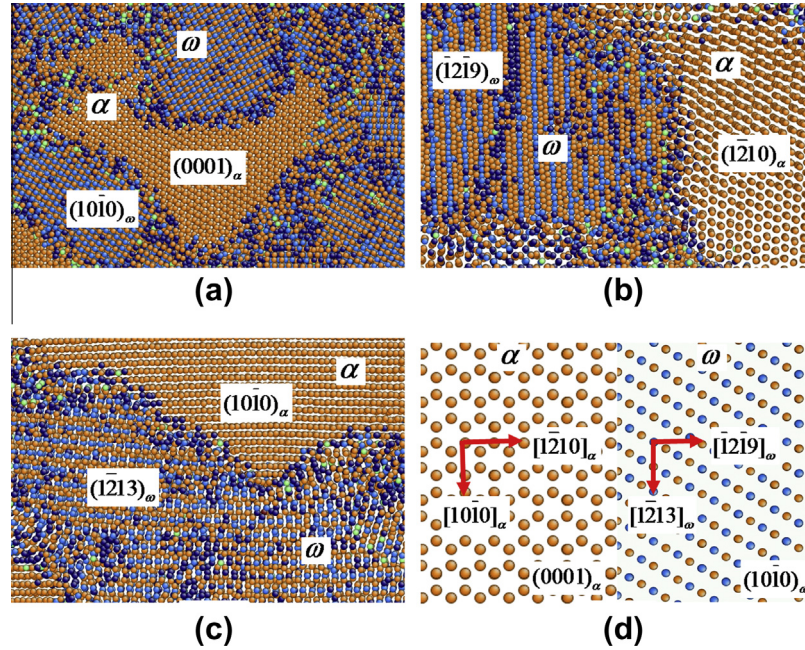


Fig. 4. Microstructural configurations showing the OR between the  $\alpha$  phase and the transformed  $\omega$  phase of the sample shocked along the  $[0001]_x$  orientation (Fig. 3a). Shown are one longitudinal cross-section (a) and two transverse cross-sections (b) and (c) (b is the same as Fig. 3a). From a knowledge of the relationships from (a)–(c), we obtain the OR  $(0001)_x // (10\bar{1}0)_\omega$  between the  $\alpha$  and  $\omega$ , as shown in (d).

results [14]. We can evaluate the crystallographic orientations of coexisting  $\alpha$  and  $\omega$  phases during the phase transformation. We have selected in Fig. 4 atomic configurations containing both parent and product phases from three normal directions. Indexing of the parallel atomic stacking planes has shown that the arrangement of the two lattices for  $\alpha$  and  $\omega$  in Fig. 4a–c leads to the ORs  $(0001)_x // (10\bar{1}0)_\omega$  and  $[10\bar{1}0]_x // [11\bar{2}3]_\omega$ , i.e. similar to those proposed by Song and Gray [14] for Zr. The orientations between the lattices in Fig. 4d match rather well; thus, a small amount of shuffle and shear facilitates the transformation.

Pathways for martensitic phase transformations can be separated into strain (a global shape change) and shuffle (small atomic relaxations) modes. There are infinitely many unique ways to transform one crystal continuously into another, but only a few allow individual atoms to displace a small distance. In order to confirm our OR, we checked the strain and shuffle parameters between the  $\alpha$  and  $\omega$  lattices during the transformation. Fig. 5 shows the configurations of the  $(0001)_x$  and  $(10\bar{1}0)_\omega$  planes in the lattice and the atomic arrangements in the planes for the new transformation pathway. The lattice parameters for both  $\alpha$  and  $\omega$  phases are  $a_\alpha = 2.95 \text{ \AA}$  and  $c_\alpha = 4.69 \text{ \AA}$ ,  $a_\omega = 4.61 \text{ \AA}$  and  $c_\omega = 2.82 \text{ \AA}$ , respectively, and thus  $c_\alpha/a_\alpha = 1.593$  and  $c_\omega/a_\omega = 0.611$ . The new transformation pathway deduced from observed ORs involves significant atomic strains, relatively small shuffle and is a direct transformation pathway with no intermediate state. Complete conversion to the  $\omega$  structure can be demonstrated to occur by coupling a shear strain along the  $[10\bar{1}0]_\alpha$  orientation with an inner-atom shuffle. The patterns of the atomic configurations in the

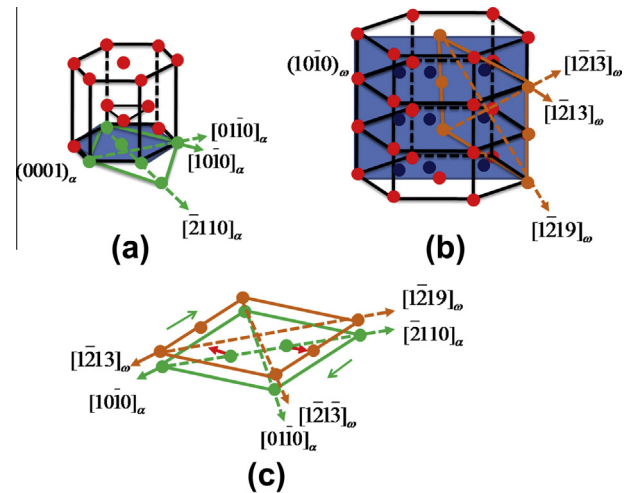


Fig. 5. Our proposed  $\alpha \rightarrow \omega$  transformation pathway for  $\alpha$ -Ti single crystal under  $c$ -axis shock compression. (a) The  $(0001)_x$  plane (green) of  $\alpha$  phase before martensitic transformation. (b) The final  $(10\bar{1}0)_\omega$  plane (orange) of  $\omega$  phase after transformation. (c) The ORs connecting the  $\alpha$  and  $\omega$  phases are  $(0001)_x // (10\bar{1}0)_\omega$  and  $[10\bar{1}0]_x // [11\bar{2}3]_\omega$ . (For interpretation of the references to color in this figure legend, the reader is referred to the web version of this article.)

$(0001)_x$  and  $(10\bar{1}0)_\omega$  planes are superimposed in Fig. 5c according to the OR. It can be seen that only a simple shear is needed to transform one lattice to the other. The lattice shearing direction is parallel to the  $[10\bar{1}0]_\alpha$  or  $[11\bar{2}3]_\omega$  directions, which switches atoms along the  $[2110]_\alpha$  axis in the  $\alpha$  phase to positions along  $[1\bar{2}19]_\omega$  in the  $\omega$  phase. In addition, the global shape change is accompanied by small movements of two inner atom shuffles in opposite

directions to effectively collapse closely spaced  $(10\bar{1}0)_\omega$  planes, as shown by arrows in Fig. 5c.

### 3.3. Shock-induced $\alpha \rightarrow \omega$ transformation along the $a$ -axis

Contrary to the shock response along  $[0001]$  direction, the microstructure evolution of Ti single crystals is more complex when shocked along the  $[10\bar{1}0]$  and  $[1\bar{2}10]$  directions. The  $\alpha \rightarrow \omega$  transformation takes place in two steps, which include an effective  $90^\circ$  reorientation and a subsequent phase transformation. In addition, the transformation pathway is different from that along the  $c$ -axis above. It is important to note that for pure Ti polycrystals, the results of shock experiments show a decrease in the velocity gradient in the compression wave instead of a double-shock configuration above the Hugoniot elastic limit (HEL) [29,30]. Razorenov et al. proposed that the steepness of the lower parts of the observed compression wave in Ti is governed by the shear viscosity, whereas the steepness of the upper part is determined by both the shear viscosity and the kinetics of the transformation [29]. Our simulation results suggest an underlying mechanism at the atomic level in which the steepness decrease of the velocity profile is determined by the coupling of the reorientation processes to phase transformation.

#### 3.3.1. Dynamics of $90^\circ$ rotation

A quantitative analysis of the transformation mechanisms was carried out for the  $[10\bar{1}0]$  and  $[1\bar{2}10]$  shock directions. We observe first a  $90^\circ$  rotation as the shock front passes the transformation region. The rotation is the result of a shear and shuffle mechanism, analogous to the  $90^\circ$  domain wall rearrangement that occurs in PZT ceramics [31,32]. Fig. 6 illustrates the mechanism of rotation from  $(0001)$ -hcp to  $(10\bar{1}0)$ -hcp. The shear along the  $\langle 10\bar{1}1 \rangle$  direction changes the global shape by a strain  $e_{xx} = -0.08$  along  $[0001]_x$  and  $e_{zz} = 0.08$  along  $[10\bar{1}0]_x$ . Meanwhile, the atomic shuffle occurs by small movements of atoms as shown by arrows in Fig. 5a.

For shock loading along the  $[10\bar{1}0]$  orientation, all the  $[10\bar{1}0]$ -hcp rotates to one type of  $[0001]$ -hcp variant with an incoherent twin boundary (ITB), as shown in Fig. 7a. However, Fig. 7c shows two different types of rotated  $[0001]$ -hcp variants along the  $[1\bar{2}10]$  shock direction, and the angle between the two variants is rounded to  $60^\circ$ . Similarly, the boundaries between the rotated and unrotated regions are ITBs, whereas a coherent twin boundary (CTB) exists between two rotated variants. The difference can be illustrated as follows: the  $[1\bar{2}10]$  shock direction forces the  $[10\bar{1}0]$ -oriented hcp to rotate to  $[0001]$ -oriented hcp. This occurs in two ways as shown in Fig. 7d. However, the  $[10\bar{1}0]$  shock direction can only give rise to the  $[0001]$ -rotated hcp as in Fig. 7b.

As for translation, rotation represents one of the principal mechanisms of plastic flow. Rotations are characteristic of a crystal lattice in much the same way that turbulent flow is characteristic of fluids. There are a variety of

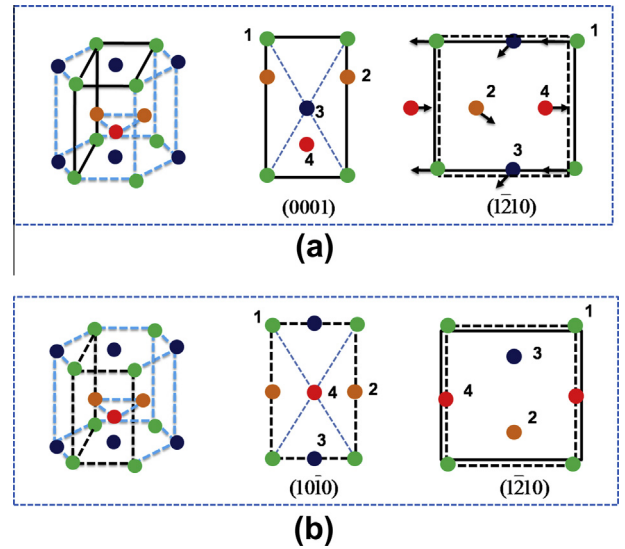


Fig. 6. Schematic illustration of the reorientation mechanism from (a)  $[0001]$ -oriented hcp to (b)  $[10\bar{1}0]$ -oriented hcp by a combination of shear and shuffle operations. In (a) are shown the basal and pyramidal planes before the reorientation. In (b) is shown the reoriented cell so that the basal and pyramidal planes in (a) become the prismatic and pyramidal planes, respectively, by a shuffling of the atoms in the directions shown. The reorientation is accompanied by a strain  $e_{xx} = 0.08$  along  $[0001]$  and  $e_{zz} = -0.08$  along  $[10\bar{1}0]$ . Each color represents a unique atom. (For interpretation of the references to color in this figure legend, the reader is referred to the web version of this article.)

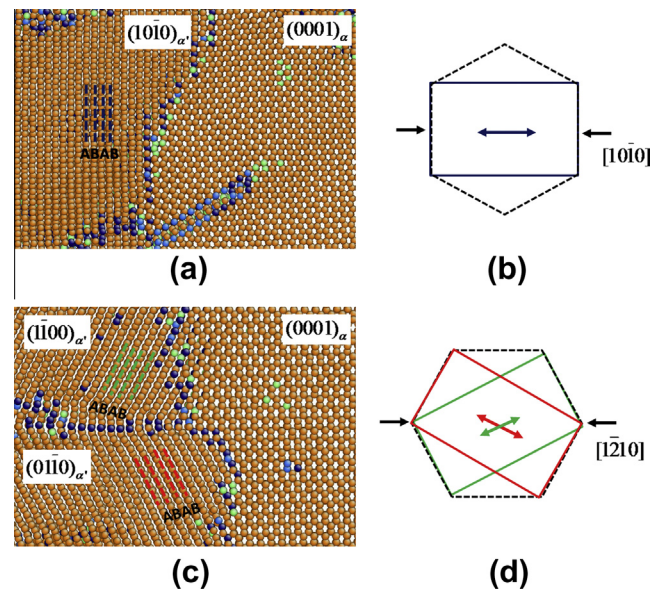


Fig. 7. The relationship between the shock direction and the number of variants of the hcp  $\alpha$  phase generated. Shock along the  $[10\bar{1}0]_x$  direction (a) and (b) leads to one variant. However, shock along the  $[1\bar{2}10]_x$  direction (c) and (d) leads to two variants.

reasons for the rotational movement in a crystalline solid. It can occur in texture formation when plastic deformation occurs on a specific plane and slip direction [33,34]. Rotational deformation, such as declinations, carried by grain boundaries significantly contribute to plastic flow in

nanomaterials [35–37]. Twinning is a particular form of rotation deformation due to atomic rearrangement. What is characteristic of twinning is the presence of special coherent boundaries separating rearranged regions, and the boundary angle has a strict fixed magnitude which is determined by the symmetry of the crystalline structure of the material. For instance, a  $90^\circ$  reorientation in a twinning–detwinning process is responsible for the spontaneous polarization rearrangement in PZT ceramics [31]. In pure Ti polycrystals, the deformation twin modes most commonly reported at RT are  $\{10\bar{1}2\}$  and  $\{11\bar{2}2\}$  for deformation parallel and perpendicular to the  $c$ -axis [38,39], respectively. The rotation angle for  $\{10\bar{1}2\}$  twins is  $85^\circ$ , close to  $90^\circ$ . However, we observe incoherent boundaries in our  $a$ -axis shocked samples. Also, no partial dislocations were observed to mediate the process. We speculate that our shear and shuffle mechanism is related to incoherent or irrational twins [40], similar to the observation of  $\{112\}$  twins in face-centered cubic Cu or Ag [41,42].

### 3.3.2. Silcock transformation pathway

Following the process of hcp variant rotation,  $\alpha$ -Ti converts subsequently to  $\omega$  phase. In order to determine the transformation mechanism, we examined the relative orientation of coexisting phases in shocked specimens. An image of an oriented thin section of the  $[10\bar{1}0]$  and  $[1\bar{2}10]$  shocked specimens with indices of the parallel crystallographic planes is shown in Fig. 8. The other ORs observed here were identified as:  $(0001)_\alpha // (1\bar{2}10)_\omega$  and  $[1\bar{2}10]_\alpha // [0001]_\omega$  or the Silcock pathway, which is consistent with the mechanics of the transformation observed by Kutsar et al. for Zr [21].

In our case, when the  $\alpha$  phase transforms to the  $\omega$  phase, there is a coordinated set of atomic shifts. The first displacement involves movement in the  $[1\bar{2}10]$  direction with a magnitude of  $0.74 \text{ \AA}$  and then in the  $[10\bar{1}0]$  direction with a magnitude  $0.204 \text{ \AA}$ . The first displacement occurs in the same manner for three neighboring atomic rows and in the opposite direction for the next three, and so on. The second displacement occurs in the opposite sense for successive  $(0001)$  planes. This transforms the  $(1\bar{2}10)_\alpha$  plane into the  $(0001)_\omega$  plane. The details of this phase transformation are given elsewhere [20]. While this OR is not predicted theoretically (the TAO-1 pathway has lower energy), it has been observed experimentally in both Ti and Zr [19,21].

### 3.4. Shear stress analysis: mechanism of anisotropic transformation

The shear stresses in the sample can be studied relative to the shock pressure. The shear stress was determined by the following equation since off-diagonal terms are negligible:

$$\tau = \frac{1}{2} \left[ \sigma_{zz} - \frac{1}{2} (\sigma_{xx} + \sigma_{yy}) \right], \quad (3)$$

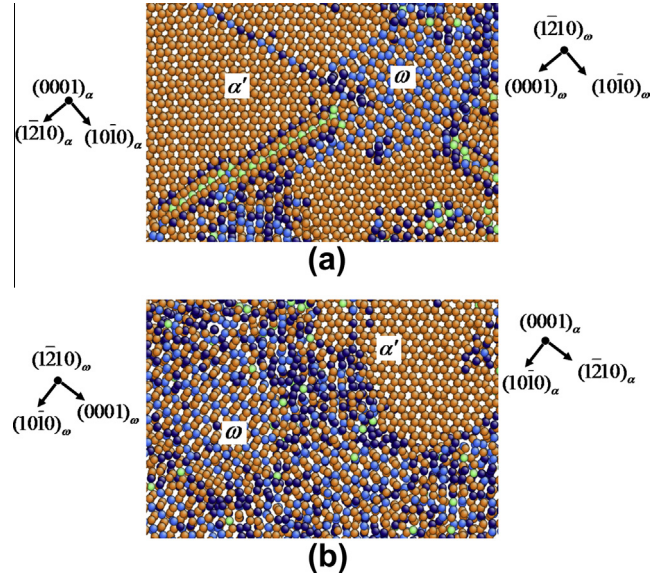


Fig. 8. Microstructure showing the OR between the reoriented  $\alpha'$  phase and transformed  $\omega$  phase along the shock directions (a)  $[10\bar{1}0]_\alpha$  and (b)  $[1\bar{2}10]_\alpha$ . The ORs connecting the  $\alpha'$  and  $\omega$  phase are the same as obtained from the Silcock relationship given by  $(0001)_\alpha // (1\bar{2}10)_\omega$  and  $[1\bar{2}10]_\alpha // [0001]_\omega$  but differ from that for shock along the  $c$ -axis (Fig. 5). The color coding and labels are the same as in Fig. 3. (For interpretation of the references to color in this figure legend, the reader is referred to the web version of this article.)

where  $\sigma_{zz}$  is the normal stress in the shock propagation direction, and  $\sigma_{xx}$  and  $\sigma_{yy}$  are transverse normal stresses. Fig. 9 shows the  $z$ -component of the stress tensor ( $\sigma_{zz}$ ) and the shear stress plotted against sample depth at 18 ps (or 22 ps) into the simulation ( $u_p = 0.9 \text{ km s}^{-1}$ ). We cannot exclude the possibility that further relaxation may take place on much longer time and distance scales than are accessible in our simulations. The different dynamics for the three different crystallographic shock directions are also

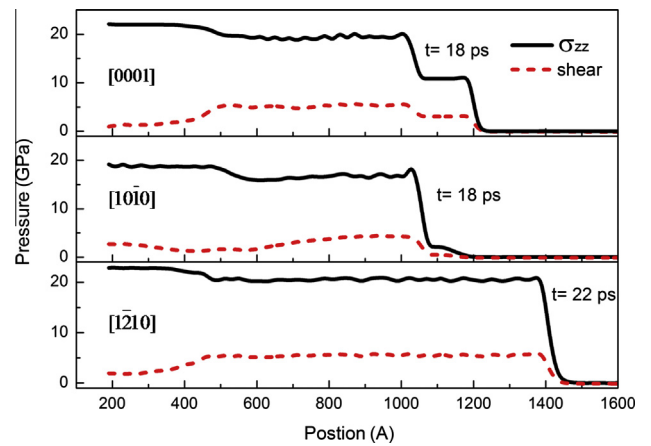


Fig. 9. Profiles of the components of the pressure tensor (longitudinal  $\sigma_{zz}$  and shear stress  $(\sigma_{zz} - (\sigma_{xx} + \sigma_{yy})/2)$ ) vs. sample depth. The shock waves (piston velocity,  $u_p = 0.9 \text{ km s}^{-1}$ ) propagate from left to right. Profiles are shown for fixed times for the three major crystallographic orientations.

reflected in the longitudinal pressure profiles, particularly in the relaxation of the shear stress.

The role of stress deviators or shear stresses is often ignored in shock-induced phase transformation studies because in most cases the yield strength is very low compared to the phase transformation stress. As pointed out by Duvall and Graham, there are notable exceptions such as CdS, InSb and quartz [25,43,44]. The shear stress effect can be characterized by a shear level parameter  $\lambda$ :

$$\lambda = \tau / \sigma_{hyd}, \quad (4)$$

where  $\tau$  is the maximum shear stress and  $\sigma_{hyd}$  is the transformation hydrostatic pressure. For dynamic high-pressure-induced phase transformation in Fe and Bi,  $\lambda < 5\%$ , whereas  $\lambda \approx 30\%$  for CdS and InSb [44–46]. In our simulation of pure Ti single crystals,  $\lambda \approx 26\%$ , which suggests that stress deviators play a significant role in the  $\alpha \rightarrow \omega$  phase transformation. Note that even under quasistatic pressure conditions, shear stress cannot be ignored during the phase transformation. For example, HPT experiments show that the application of shear stress, in addition to pressure, reduces the  $\alpha \rightarrow \omega$  transformation pressure and hysteresis [7,8,47]. Although the TAO-1 transformation pathway [16] has the lowest energy barrier under hydrostatic pressure, the Silcock mechanism is also commonly reported experimentally in both Ti and Zr. Thus, the shear stress is likely the underlying reason for the anisotropic transformation pathways we have observed for pure Ti under shock compression.

#### 4. Summary and discussion

The  $\alpha \rightarrow \omega$  phase transformation induced by shock compression of single-crystal Ti along three perpendicular directions was investigated by means of MD simulations. The sample length in the shock direction was 0.2  $\mu\text{m}$  and non-equilibrium MD was performed for up to 30 ps. The shock response along  $[0001]$ ,  $[10\bar{1}0]$  and  $[12\bar{1}0]$  in Ti provided a constitutive response consistent with Hugoniot data obtained experimentally. The shock response shows an obvious anisotropy in wave profiles, exhibiting a split three-wave structure along the  $[0001]$  and  $[10\bar{1}0]$  directions, and an overdriven two-wave profile along  $[12\bar{1}0]$ .

In contrast to the  $\alpha \rightarrow \varepsilon$  transformation in pure Fe [48,49] for which the Burgers mechanism applies, we find two different crystallographic orientation relationships between the parent and product phases. For  $c$ -axis shock compression, MD simulation results give the ORs  $(0001)_\alpha // (10\bar{1}0)_\omega$  and  $[10\bar{1}0]_\alpha // [11\bar{1}]_\omega$  between the  $\alpha$  and  $\omega$  phases. This differs from a mechanism previously proposed from Zr polycrystal shock studies. However, recent work suggests that the latter is a subset of Variant I, which has the same OR as TAO-1 but a different mechanism. Our OR is probably also a subset of Variant I. What is important is that  $\alpha$ -Ti single crystals undergo a 90° rotation and subsequent  $\alpha \rightarrow \omega$  martensitic transformation when they are subjected to shock compression along

the  $a$ -axis. This transformation pathway is consistent with the previously proposed Silcock relationship. Using nonlinear elastic stress–strain relations, we have also calculated the shear level parameter  $\lambda \approx 26\%$ , which indicates that stress deviators play a significant role in the  $\alpha \rightarrow \omega$  phase transformation. We propose a hypothesis that the anisotropy of shear stress is responsible for the anisotropic transformation pathway.

Our predicted lattice rotation, preceding the phase transformation, is a form of cooperative plastic deformation with an incoherent domain grain boundary between the unrotated and rotated parent  $\alpha$ . Although we do not focus here on the precise mechanisms involved, we expect that the characteristic signature of the rotation should be detectable by TEM or X-ray diffraction measurements. The emergence of in situ and high-resolution temporal and spatial probes (e.g. coherent diffraction using XFEL's at facilities such as LCLS), provides an excellent near-term opportunity to validate our predictions relating to the anisotropic behavior under shock environments in high-purity single crystals of Ti.

#### Acknowledgements

This work was supported by NSFC (51171140, 51231008, 51320105014, 51321003), the 973 Program of China (2010CB631003, 2012CB619402) and 111 projects (B06025), as well as the US DOE at LANL (DE-AC52-06NA25396).

#### References

- [1] Leyens C, Peters M. Titanium and titanium alloys: fundamentals and applications. New York: John Wiley & Sons; 2006.
- [2] Schutz RW, Watkins HB. Mater Sci Eng A 1998;243:305.
- [3] Geetha M, Singh AK, Asokamani R, Gogia AK. Prog Mater Sci 2009;54:397.
- [4] Williams JC, Starke Jr EA. Acta Mater 2003;51:5775.
- [5] Sikka SK, Vohra YK, Chidambaram R. Prog Mater Sci 1982;27:245.
- [6] Singh AK, Mohan M, Divakar C. J Appl Phys 1982;53:1221.
- [7] Todaka Y, Sasaki J, Moto T, Uernoto M. Scripta Mater 2008;59:615.
- [8] Errandonea D, Meng Y, Somayazulu M, Hausermann D. Physica B 2005;355:116.
- [9] Rigg PA, Greeff CW, Knudson MD, Gray GT, Hixson RS. J Appl Phys 2009;106:123532.
- [10] Hennig RG, Trinkle DR, Bouchet J, Srinivasan SG, Albers RC, Wilkins JW. Nat Mater 2005;4:129.
- [11] Cerreta E, Gray GT, Hixson RS, Rigg PA, Brown DW. Acta Mater 2005;53:1751.
- [12] Cerreta E, Gray III GT, Lawson AC, Mason TA, Morris CE. J Appl Phys 2006;100:013530.
- [13] Jyoti G, Joshi KD, Gupta SC, Sikka SK, Dey GK, Banerjee S. Philos Mag Lett 1997;75:291.
- [14] Song SG, Gray GT. Philos Mag A 1995;71:275.
- [15] Jyoti G, Tewari R, Joshi KD, Srivastava D, Dey GK, Gupta SC, et al. Defect Diffus Forum 2008;279:133.
- [16] Trinkle DR, Hennig RG, Srinivasan SG, Hatch DM, Jones MD, Stokes HT, et al. Phys Rev Lett 2003;91:025701.
- [17] Usikov MP, Zilbersh Va. Phys Status Solidi A 1973;19:53.
- [18] Vohra YK, Sikka SK, Menon ESK, Krishnan R. Acta Metall 1980;28:683.

- [19] Rabinkin A, Talianker M, Botstein O. *Acta Metall* 1981;29:691.
- [20] Silcock JM. *Acta Metall* 1958;6:481.
- [21] Kutsar AR, Lyasotski IV, Podurets AM, Sanches-bolinches AF. *High Pressure Res* 1990;4:475.
- [22] Plimpton S. *J Comput Phys* 1995;117:1.
- [23] Lenosky TJ, Sadigh B, Alonso E, Bulatov VV, de la Rubia TD, Kim J, et al. *Modell Simul Mater Sci Eng* 2000;8:825.
- [24] Marsh SP. *Lasl shock hugoniot data*. University of California Press; 1980.
- [25] Duval GE, Graham RA. *Rev Mod Phys* 1977;49:523.
- [26] Eliezer S, Gilath I, Barnoy T. *J Appl Phys* 1990;67:715.
- [27] Jidong Y, Wenqiang W, Qiang W. *Phys Rev Lett* 2012;109:115701.
- [28] Germann TC, Holian BL, Lomdahl PS, Ravelo R. *Phys Rev Lett* 2000;84:5351.
- [29] Razorenov SV, Utkin AV, Kanel GI, Fortov VE, Yarunichev AS, Baumung K, et al. *High Pressure Res* 1995;13:367.
- [30] Kanel GI, Razorenov SV, Zaretsky EB, Herrman B, Meyer L. *Phys Solid State* 2003;45:656.
- [31] Lente MH, Eiras JA. *J Appl Phys* 2001;89:5093.
- [32] Ivry Y, Wang N, Chu D, Durkan C. *Phys Rev B* 2010;81.
- [33] Margulies L, Winther G, Poulsen HF. *Science* 2001;291:2392.
- [34] Dillamore IL, Roberts WT. *Acta Metall* 1964;12:281.
- [35] Trautt ZT, Mishin Y. *Acta Mater* 2012;60:2407.
- [36] Gorkaya T, Molodov KD, Molodov DA, Gottstein G. *Acta Mater* 2011;59:5674.
- [37] Murayama M, Howe JM, Hidaka H, Takaki S. *Science* 2002;295:2433.
- [38] Chichili DR, Ramesh KT, Hemker KJ. *Acta Mater* 1998;46:1025.
- [39] Battaini M, Pereloma EV, Davies CHJ. *Metal Mater Trans A* 2007;38A:276.
- [40] Partridge PG, Roberts E. *Acta Metall* 1964;12:1205.
- [41] Liu L, Wang J, Gong SK, Mao SX. *Phys Rev Lett* 2011;106:175504.
- [42] Han WZ, An Q, Luo SN, Germann TC, Tonks DL, Goddard III WA. *Phys Rev B* 2012;85:024107.
- [43] Kusaba K, Kikuchi M, Fukuoka K, Syono Y. *Phys Chem Miner* 1988;15:238.
- [44] Sharma SM, Gupta YM. *Phys Rev B* 1998;58:5964.
- [45] Knudson MD, Gupta YM, Kunz AB. *Phys Rev B* 1999;59:11704.
- [46] Tang ZP, Gupta YM. *J Appl Phys* 1997;81:7203.
- [47] Zilbershtein VA, Chistotina NP, Zharov AA, Grishina NS, Estrin EI. *Phys Metal Mettalogr* 1975;39:445.
- [48] Kadau K, Germann TC, Lomdahl PS, Holian BL. *Science* 2002;296:1681.
- [49] Kadau K, Germann TC, Lomdahl PS, Holian BL. *Phys Rev B* 2005;72.